

Tracking Hadean processes in modern basalts with ^{142}Nd -NeodymiumM.F. Horan^{a,*}, R.W. Carlson^a, R.J. Walker^b, M. Jackson^c, M. Garçon^d, M. Norman^e^a Department of Terrestrial Magnetism, Carnegie Institution for Science, 5241 Broad Branch Road, NW 20015, USA^b Department of Geology, University of Maryland, College Park, MD 20742, USA^c Department of Earth Science, University of California, Santa Barbara, CA 93106, USA^d ETH Zürich, Department of Earth Sciences, Institute of Geochemistry and Petrology, Clausiusstrasse 25, 8092 Zürich, Switzerland^e Research School of Earth Sciences, The Australian National University, Canberra ACT 0200, Australia

ARTICLE INFO

Article history:

Received 18 July 2017

Received in revised form 5 December 2017

Accepted 10 December 2017

Available online 22 December 2017

Editor: F. Moynier

Keywords:

ocean island basalt

 ^{142}Nd

mantle heterogeneity

Hadean differentiation

Hawaii

Samoa

ABSTRACT

The short-lived $^{146}\text{Sm} \rightarrow ^{142}\text{Nd}$ isotope system ($t_{1/2} = 103$ Ma) provides constraints on the timing and processes of terrestrial silicate fractionation during the early Hadean. Although some Archean terranes preserve variability in $^{142}\text{Nd}/^{144}\text{Nd}$, no anomalies have been resolved previously in young rocks. This study provides high precision $^{142}\text{Nd}/^{144}\text{Nd}$ data on a suite of ocean island basalts from Samoa and Hawaii previously shown to have variable depletions in $^{182}\text{W}/^{184}\text{W}$ that are inversely correlated with $^3\text{He}/^4\text{He}$ ratios. Improved analytical techniques and multiple replicate analyses of Nd show a variation in $\mu^{142}\text{Nd}$ values between -1.3 and $+2.7$ in the suite, relative to the JNdi standard. Given the reproducibility of the standard (± 2.9 ppm, 2 SD), two Samoan samples exhibit resolved variability in their $^{142}\text{Nd}/^{144}\text{Nd}$ ratios outside of their 95% confidence intervals, suggesting minor variability in the Samoan hotspot. One sample from Samoa has a higher $\mu^{142}\text{Nd}$ of $+2.7$, outside the 95% confidence interval (± 1.0 ppm) of the average of the JNdi standard. Limited, but resolved, variation in $^{142}\text{Nd}/^{144}\text{Nd}$ within the suite suggests the preservation of early Hadean silicate differentiation in the sources of at least some basalts from Samoa. Larger variations of $^{182}\text{W}/^{184}\text{W}$ and $^3\text{He}/^4\text{He}$ ratios in the same samples suggest that metal–silicate separation and mantle outgassing left a more persistent imprint on the accessible mantle compared to $^{142}\text{Nd}/^{144}\text{Nd}$ ratios which are impacted by early silicate differentiation.

© 2017 Elsevier B.V. All rights reserved.

1. Introduction

Modern oceanic basalts preserve variations in the relative abundance of the daughter products of short-lived radioactive isotopes that reflect chemical differentiation processes occurring in the early Hadean (Mukhopadhyay, 2012; Rizo et al., 2016; Mundl et al., 2017). These isotopic tools track different processes involved in Earth's earliest differentiation. For example, the ratios $^{129}\text{Xe}/^{130}\text{Xe}$ ($^{129}\text{I} \rightarrow ^{129}\text{Xe}$, $t_{1/2} = 15$ Ma) in some mid-ocean ridge basalts (MORB) and ocean island basalts (OIB) indicate that the source reservoirs for MORB and OIB experienced different outgassing histories and were isolated from each other within the first 100 Ma of Earth history (Mukhopadhyay, 2012; Pető et al., 2013; Parai and Mukhopadhyay, 2015). The short-lived $^{182}\text{Hf} \rightarrow ^{182}\text{W}$ isotope system ($t_{1/2} = 8.9$ Ma) is sensitive to both early

Hadean metal–silicate differentiation and silicate–liquid fractionation, as Hf is lithophile and less incompatible during silicate melting, compared to W, which is also moderately siderophile. Ocean island basalts from Samoa and Hawaii show variable depletions in $^{182}\text{W}/^{184}\text{W}$ that are negatively correlated with their $^3\text{He}/^4\text{He}$ ratios (Mundl et al., 2017). By contrast, the 60 Ma basalts from Baffin Bay, Canada, characterized by the highest known $^3\text{He}/^4\text{He}$ ratios in terrestrial rocks, show elevated $^{182}\text{W}/^{184}\text{W}$ ratios (Rizo et al., 2016). The causes of these variations are not yet clear, with suggested explanations including sources differentially affected by the late addition of gas- and siderophile-rich meteoritic components following core formation (e.g. Willbold et al., 2011), early-differentiated sources that could include core metal (e.g. Porcelli and Halliday, 2001), or deep, undegassed, remnants of early Earth differentiation events, possibly located in seismically anomalous zones near the core–mantle boundary (e.g. Coltice et al., 2011; Mundl et al., 2017).

The short-lived $^{146}\text{Sm} \rightarrow ^{142}\text{Nd}$ system ($t_{1/2} = 103$ Ma, Appendix A1, Section S1) would be affected by early Hadean differentiation of the silicate Earth, like the ^{182}Hf – ^{182}W system. An important difference between the Sm–Nd and Hf–W systems, how-

* Corresponding author.

E-mail addresses: mhoran@carnegiescience.edu (M.F. Horan), rcarlson@carnegiescience.edu (R.W. Carlson), rjwalker@umd.edu (R.J. Walker), jackson@geol.ucsb.edu (M. Jackson), marion.garcon@erdw.ethz.ch (M. Garçon), marc.norman@anu.edu.au (M. Norman).

Table 1
Faraday cup configuration for multidynamic analysis of Nd.

	L4	L3	L2	L1	C	H1	H2	H3	H4
Step 1		(140)	(141)	142	143	144	145	146	(147)
Step 2	(140)	(141)	142	143	144	145	146	(147)	148
Step 3	(141)	142	143	144	145	146	(147)	148	(149)
Step 4	142	143	144	145	146	(147)	148	(149)	150

ever, is that neither Sm or Nd are siderophile, unlike W, hence the Sm–Nd system is insensitive to metal–silicate separation. Even small changes (e.g., 5%) in Sm/Nd ratios by silicate melting and crystal–liquid fractionation during the first few hundred million years of Earth’s history should result in measurable (c. 10 ppm) offsets in $^{142}\text{Nd}/^{144}\text{Nd}$ ratios between melt and residue and/or cumulate. Consistent with this prediction, enrichments and depletions of up to 20 ppm in $^{142}\text{Nd}/^{144}\text{Nd}$ have been measured in rocks from early Earth terranes, indicating that the oldest preserved crust was derived from sources that experienced differentiation in the Hadean (Caro et al., 2006; Bennett et al., 2007; O’Neil et al., 2008; Rizo et al., 2012, 2013; Morino et al., 2017). The magnitude of ^{142}Nd anomalies in ancient rocks appears to have decreased with time during the Archean, and has been interpreted as evidence that early fractionated mantle domains were mixed away by the end of the Archean (Rizo et al., 2012; Debaille et al., 2013).

In modern rocks, no variations in $^{142}\text{Nd}/^{144}\text{Nd}$ have been resolved outside of an uncertainty of, at minimum, ± 5 ppm (Boyet and Carlson, 2006; Caro et al., 2006; Jackson and Carlson, 2012; Murphy et al., 2010; Rizo et al., 2016; de Leeuw et al., 2017). Whether ^{142}Nd variations in the sources of modern rocks have been homogenized through >4.5 Ga of mantle convection, hide within the analytical uncertainties of previous measurements, or reside in rocks not yet analyzed is unknown. For this study, our approach targeted a small sample suite of OIB from Samoa and Hawaii that show variability in W and He isotope compositions (Mundl et al., 2017). Our specific aim was to evaluate whether any samples that have anomalies in $^{182}\text{W}/^{184}\text{W}$ might also have resolvably different $^{142}\text{Nd}/^{144}\text{Nd}$. In order to increase the level of analytical resolution, we refined procedures for Nd purification and isotopic analysis, and performed multiple replicate analyses of each sample to reduce the uncertainty on the $^{142}\text{Nd}/^{144}\text{Nd}$ composition of each sample, and to better understand the earliest silicate fractionation history of OIB sources.

2. Methods

Sample aliquots for this study were taken from the same powders used in Mundl et al. (2017), in order to circumvent uncertainties from sample heterogeneity. These samples are described in Appendix A1, Section S2. Approximately 100 mg of powder was dissolved in HF–HNO₃ in a closed PFA beaker at 130 °C. Samples were dried, and re-dissolved successively in concentrated HNO₃ and HCl until a clear solution without precipitates was obtained. We used a four-column procedure to purify Nd. First, the rare earth element (REE) fraction was separated from major elements in 6 M HCl using 2 mL of BioRad AG50Wx8 cation exchange resin. Cerium was removed from the REE fraction next using oxidative chromatography after Hirahara et al. (2012). In this procedure, Ce in the REE fraction was oxidized in a solution of 10 M HNO₃ + 20 mM NaBrO₃ and adsorbed onto 0.5 mL of Eichrom LN resin (50–100 micron), while the trivalent REE were eluted and collected. This column procedure was repeated. From the resulting Ce-free REE fraction, sodium was removed using a protocol similar to that used for the first group REE separation. Lastly, Nd was separated from the REE fraction on PFA columns using a 12 cm by 0.4 cm bed of Eichrom LN resin (20–50 micron) and 0.17–0.20 M HCl. This

purification scheme yielded undetectable Sm, $^{140}\text{Ce}/^{144}\text{Nd}$ ratios $<3 \times 10^{-6}$ and $^{141}\text{Pr}/^{144}\text{Nd} <1.0$. Recoveries of Nd were between 75% and $>90\%$. Prior to analysis by thermal ionization mass spectrometry (TIMS), 1% of the final Nd fraction was measured on a Thermo iCAP-Q quadrupole ICP-mass spectrometer to determine the amount of Nd recovered, and to verify the absence of Ce and Sm.

Neodymium was analyzed using double Re filaments on a Thermo Triton TIMS instrument at the Department of Terrestrial Magnetism, Carnegie Institution for Science. The amount of Nd loaded onto the filament was controlled to between 600–800 ng, and the intensity of ^{142}Nd was maintained between 3 to 6×10^{-11} A during analysis. The Faraday cup configuration for multidynamic analysis is shown in Table 1. A 4-step analysis program rotated masses 143, 144, 145 and 146 into the center cup and, for each cycle, yielded two dynamic ratios for $^{142}\text{Nd}/^{144}\text{Nd}$, as well as two dynamic ratios each for $^{143}\text{Nd}/^{144}\text{Nd}$ and $^{148}\text{Nd}/^{144}\text{Nd}$, and three dynamic ratios for $^{145}\text{Nd}/^{144}\text{Nd}$. Dynamic ratios for $^{150}\text{Nd}/^{144}\text{Nd}$ were not calculated with this method, so static $^{150}\text{Nd}/^{144}\text{Nd}$ ratios are shown in the Appendix A2, Supplemental Table. Intensities of ^{140}Ce and ^{147}Sm were measured and used to correct for interferences on Nd isotopes; ^{141}Pr was also monitored. A typical analysis of a given filament included 300–900 cycles and provided 600–1800 dynamic $^{142}\text{Nd}/^{144}\text{Nd}$ ratios. On-peak integration times were 8 s. Once every five blocks of 30 cycles, peaks were centered, the source was tuned and baselines were collected for 30–300 s. Amplifiers were not electronically rotated between blocks, although amplifier gains were calibrated each day.

Mass spectrometry data were reduced offline using baseline corrected intensities for each isotope. Mass fractionation was corrected using $^{146}\text{Nd}/^{144}\text{Nd} \equiv 0.7219$ and applying an exponential equation. Ratios for $^{146}\text{Nd}/^{144}\text{Nd}$ typically increased throughout an analysis. Multidynamic ratios normally would be calculated using $^{146}\text{Nd}/^{144}\text{Nd}$ obtained during a different time step within a 4-step cycle. For example, to dynamically correct the $^{142}\text{Nd}/^{144}\text{Nd}$ measured in step 1 (using Faraday cups L1 and H1), our analysis routine uses the ratio for $^{146}\text{Nd}/^{144}\text{Nd}$ collected in step 3 (in the same cups). To better accommodate changing fractionation with time, we instead used a $^{146}\text{Nd}/^{144}\text{Nd}$ ratio interpolated (using a linear interpolation) from that measured in step 3 within the same cycle and from the previous cycle. Similarly, dynamic ratios for $^{143}\text{Nd}/^{144}\text{Nd}$, $^{145}\text{Nd}/^{144}\text{Nd}$ and $^{148}\text{Nd}/^{144}\text{Nd}$ were calculated using time-corrected $^{146}\text{Nd}/^{144}\text{Nd}$. The equations used for the exponential mass fractionation correction of these multidynamic ratios are given in Appendix A1, Section S3. Dynamic ratios calculated in this way eliminated inverse correlations between dynamic $^{142}\text{Nd}/^{144}\text{Nd}$ and $^{148}\text{Nd}/^{144}\text{Nd}$ ratios within a given analysis (Fig. 1) and among different analyses (Fig. 2), and reduced the systematic bias in the final average ratios of $^{142}\text{Nd}/^{144}\text{Nd}$, $^{143}\text{Nd}/^{144}\text{Nd}$, $^{145}\text{Nd}/^{144}\text{Nd}$ and $^{148}\text{Nd}/^{144}\text{Nd}$ that resulted from changing mass fractionation during the individual analyses. Two analyses of the JNdi standard that underwent the same chemical purification procedures as the samples are noted in the Appendix A2, Supplemental Table and showed no detectable isotopic effects resulting from purification.

3. Results

In order to better evaluate if differences in $^{142}\text{Nd}/^{144}\text{Nd}$ ratios could be resolved among the rock samples chosen for this study,

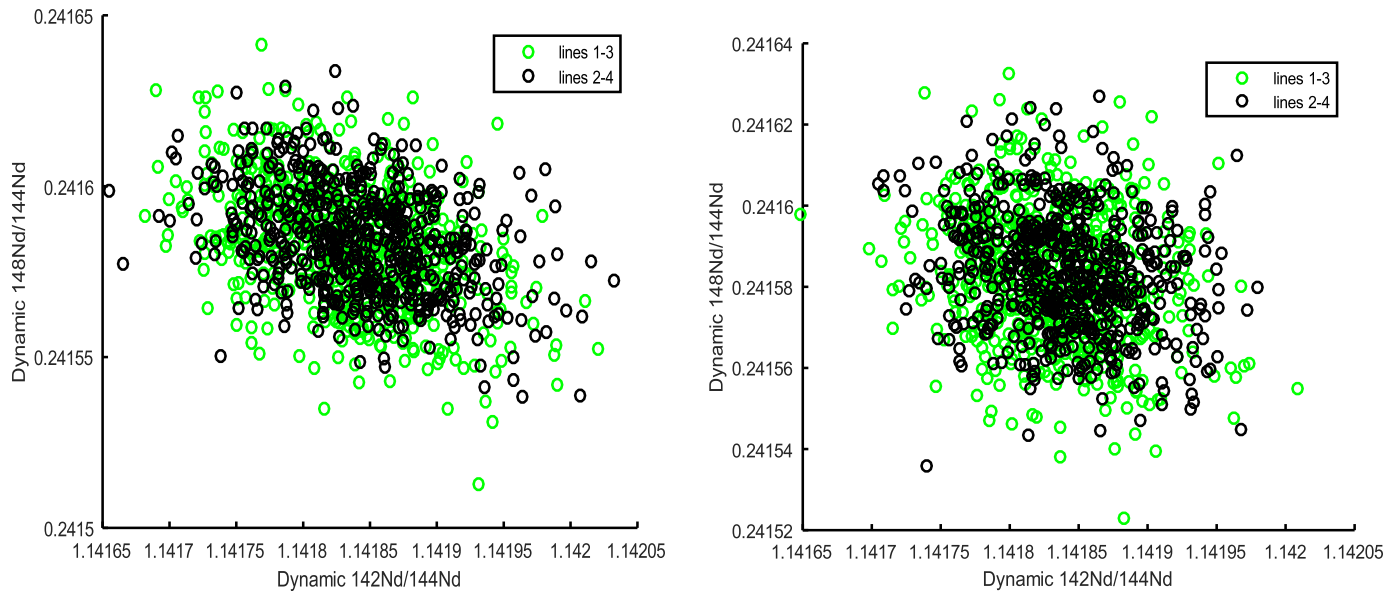


Fig. 1. Moving averages ($N = 20$) of dynamically corrected ratios of $^{142}\text{Nd}/^{144}\text{Nd}$ and $^{148}\text{Nd}/^{144}\text{Nd}$ from a single analysis of JNdi (a) normalized for mass fractionation using the $^{146}\text{Nd}/^{144}\text{Nd}$ ratio measured in the same cycle and (b) normalized using a time-corrected $^{146}\text{Nd}/^{144}\text{Nd}$ ratio interpolated from that measured within the same cycle and one from the previous cycle.

we performed both replicate chemical dissolutions and replicate mass spectrometric analyses utilizing different filaments. The full Nd dataset for individual mass spectrometric analyses of samples and standards is provided in the Appendix A2, Supplemental Table. An individual analysis consists of data obtained from one filament; measurement precision for an individual analysis is provided as 2 SE. Ratios for $^{142}\text{Nd}/^{144}\text{Nd}$ are given as $\mu^{142}\text{Nd}$, which are the deviations in parts per million (ppm) from the weighted average of JNdi standard analyses.

A weighted average was calculated for repeated measurements ($N = 12$) of 600 ng of the JNdi standard over the course of the analytical campaign. This weighted average gave 2 standard deviations = ± 2.9 ppm for $^{142}\text{Nd}/^{144}\text{Nd}$ ratios, which represents the best precision that might be expected for a single analysis of a sample or standard. The 95% confidence interval for this set of measurements of JNdi is ± 1.0 ppm which is an estimate for the best precision that can be achieved by combining the results from multiple analyses. The 95% confidence interval is calculated using:

$$\frac{1SD}{\sqrt{N}} * t_{1-\frac{\alpha}{2}, 2N-2}$$

where 1 SD is the standard deviation of the set of replicate analyses, N is the number of analyses, and t is the Student's t factor for a significance level, α , in which $\alpha = 0.05$ and the degrees of freedom is $2N - 2$ (Ludwig, 2008). In the equation above, α is divided by 2 to provide the cumulative probability for a two-sided test because it is not known if the “true” value is higher or lower than the average (NIST/SEMATECH, 2012). For our standards data, as well any dataset in which the probability of fit (chi square distribution) of the individual analyses is higher than 0.15, the dominant contributor to the uncertainty of the weighted average is the measurement errors of the individual analyses. The 95% confidence interval for such high probabilities of fit is similar to the error-weighted uncertainty given by

$$\frac{1}{\sqrt{\sum \frac{1}{2SE_i^2}}}$$

Table 2

Weighted means for each sample and 95% confidence intervals.

	$\mu^{142}\text{Nd}$	95% conf.	Probability of fit	N
Samoa				
ALIA 115-18	0.5	1.0	0.64	5
OFU 04-14	2.7	1.3	0.88	5
OFU-04-15	0.3	3.0	0.10	4
T33	-1.3	1.5	0.96	4
Hawaii				
J2-374-R5-A	-0.7	2.6	0.04	5
LO-02-02	2.6	1.7	0.33	3
ML 1868-9	-0.5	2.3	0.16	5

95% confidence intervals: see text for explanation.

Probability of fit: Chi square calculated using 2 SE measurement uncertainties for individual analyses.

N : number of individual analyses included in average. Full dataset is in the Appendix A2, Supplemental Table.

where 2 SE is the measurement uncertainty for each analysis, i . For probabilities of fit < 0.15 for a set of individual replicate analyses, however, equation 2 will underestimate the error on the weighted mean, so equation 2 was not used to calculate the uncertainties on averages in this study. Following Ludwig (2008), we use the more conservative 95% confidence intervals to report the uncertainty of the weighted averages of sample replicates.

Each sample in this study has 3–5 replicate analyses. Results for individual analyses of each sample are shown in Fig. 3. Replicate analyses and their individual measurement precisions (2SE) are combined to give a weighted average $\mu^{142}\text{Nd}$ for each sample and a corresponding uncertainty at the 95% confidence level (Table 2 and Fig. 4). All the samples in this study have $\mu^{142}\text{Nd}$ values between -1.3 and $+2.7$, with their individual 95% confidence intervals between ± 1.0 and ± 3.2 ppm. The total range of $\mu^{142}\text{Nd}$ reported here for these samples is smaller than measured in most previous studies of young terrestrial rocks (Boyett and Carlson, 2006; Murphy et al., 2010; Jackson and Carlson, 2012; Rizo et al., 2016; de Leeuw et al., 2017), except for those reported in Caro et al. (2006).

Unlike prior studies of $^{142}\text{Nd}/^{144}\text{Nd}$, we sought to reduce analytical uncertainties by multiple analysis of a given sample. The improvement in precision in this study largely results from a com-

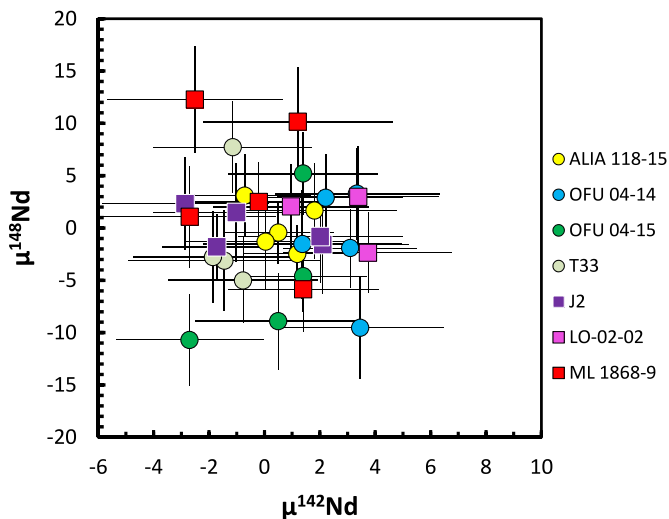


Fig. 2. Data for $\mu^{142}\text{Nd}$ vs. $\mu^{148}\text{Nd}$ for the individual analyses of samples from Hawaii (squares) and Samoa (circles) in this study. Error bars are 2 SE for each analysis. **No correlation is observed between these isotope ratios** either for replicates analyses of same rock sample or for the whole dataset.

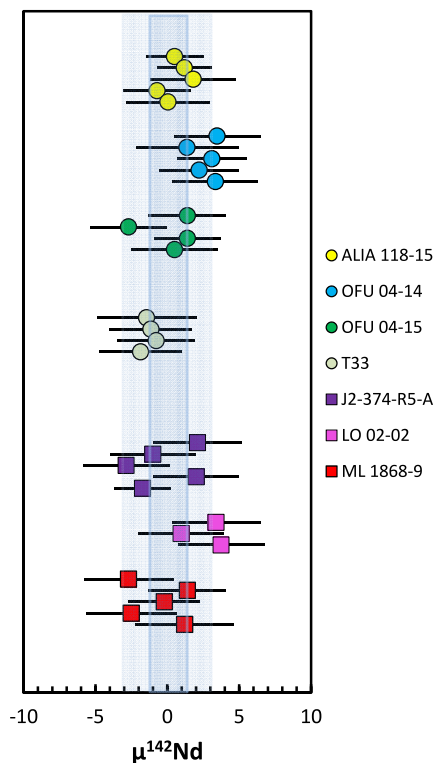


Fig. 3. Results for $^{142}\text{Nd}/^{144}\text{Nd}$ of individual analyses of samples from Samoa (circles) and Hawaii (squares). Each symbol represents the results from analysis of one filament. The lighter field is 2 SD of analyses ($N = 12$) of 600 ng of the JNdi standard; the darker field is the 95% confidence interval for the weighted average of the standard analyses.

bination of a more accurate correction for mass bias and of more multidynamic data for each sample, both from longer individual analyses and more replicates. Use of 95% confidence level to describe the precision of the weighted average composition of each sample allows more robust comparison of the sample compositions. Consequently, results reported here are not easily compared with results from prior studies. To further constrain accuracy and precision of sample analyses, one of the basalt samples (ALIA 118-15) was artificially enriched with a known amount of ^{142}Nd

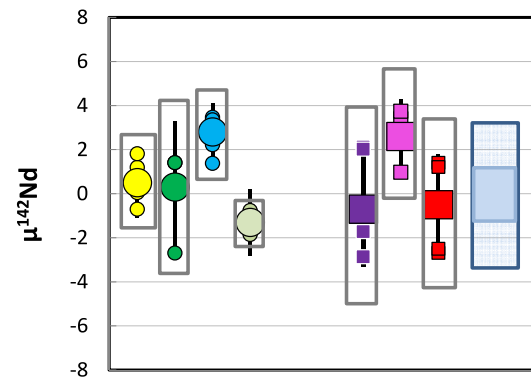


Fig. 4. Combined results for $^{142}\text{Nd}/^{144}\text{Nd}$ given as ppm deviation for the average JNdi standard value. Individual mass spectrometric analyses are shown as small circles (Samoa) and squares (Hawaii), some of which are partially hidden beneath the larger symbols. Large symbols for each sample are the calculated weighted average for the individual analyses; error bars on these averages are 95% confidence intervals; boxes enclosing each sample's data are 2 SD of the weighted average. Results for 600 ng loads of JNdi are given on the right, in which the larger region is 2 SD and the smaller, darker region is the 95% confidence interval.

and then processed through chemistry and mass spectrometry using the procedures described above. The procedures and results of this experiment are described in Appendix A1, Section S4 and in Appendix A2 Supplemental Table. This experiment confirms that, for our method, both random and systematic errors in measured $^{142}\text{Nd}/^{144}\text{Nd}$ are within our stated precisions.

All seven samples chosen for this study had $\mu^{142}\text{Nd}$ within the 2SD of the JNdi standard (± 2.9 ppm). Four of the samples examined here have $\mu^{142}\text{Nd}$ within the 95% confidence interval of the JNdi standard (± 1.0 ppm). One basalt from the Samoan island of Ofu (Ofu-04-14) has a $\mu^{142}\text{Nd}$ value of $+2.7 \pm 1.3$ which is higher than, and outside of the 95% confidence interval, of the value for JNdi. Of greatest note, a small (c. 4 ppm) difference is resolved between this basalt and a basalt from the Samoan island of Ta'u (T33, -1.3 ± 1.5). The average of the other sample from Ofu (OFU 04-15, $+0.6 \pm 3.2$), however, has a larger uncertainty that overlaps both T33 and OFU 04-14. Loihi sample LO-02-02 has a nominal $\mu^{142}\text{Nd}$ value similar to Ofu-04-14, but a larger 95% confidence interval. Therefore, no $\mu^{142}\text{Nd}$ values among the samples from Hawaii are resolved from one another, outside of their 95% confidence intervals.

4. Discussion

4.1. Hadean vs. later processes

The samples in this study show a total variation in $\mu^{142}\text{Nd}$ that is quite small (< 4 ppm) in spite of the fact that the samples span a large fraction of the range of W and He isotope compositions observed in these OIB systems (Mundl et al., 2017). Nevertheless, the sample having 2.7 ppm higher $^{142}\text{Nd}/^{144}\text{Nd}$ than the JNdi average, albeit near the limit of our resolution, is also characterized by a $^3\text{He}/^4\text{He}$ ratio that is among the highest, and $\mu^{182}\text{W}$ values that are among the lowest, of the Samoan suite (Fig. 5), although not all of the high $^3\text{He}/^4\text{He}$ and low $\mu^{182}\text{W}$ lavas have resolvable ^{142}Nd anomalies. Because some high $^3\text{He}/^4\text{He}$, low $\mu^{182}\text{W}$ samples from Samoa and Hawaii show evidence for early Hadean fractionation of Hf/W within the lifetime of ^{182}Hf , these samples are particularly useful to evaluate whether their Nd isotope systematics are consistent with a similar early fractionation of Sm/Nd. Further, the combination of the long-lived system $^{147}\text{Sm} \rightarrow ^{143}\text{Nd}$ ($t_{1/2} = 106$ Ga) with the short-lived $^{146}\text{Sm}-^{142}\text{Nd}$ system offers the opportunity to separate the chemical consequences of early Earth differentiation events from those occurring later in Earth history, for example

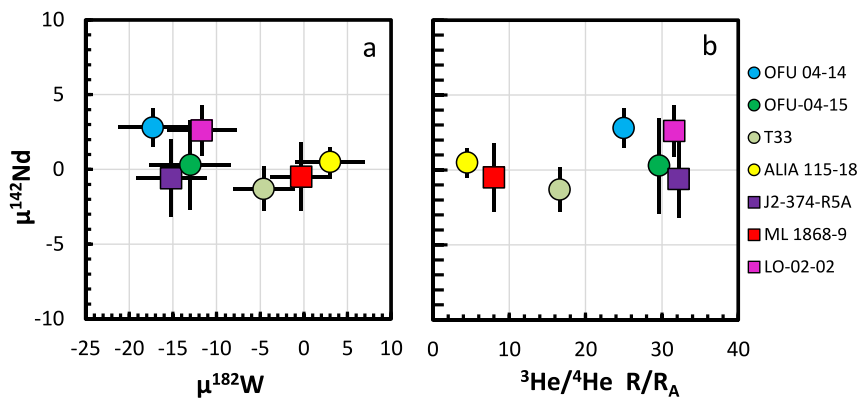


Fig. 5. (a) Plot of $\mu^{142}\text{Nd}$ vs. $\mu^{182}\text{W}$ (Mundl et al., 2017). Tungsten isotope data for OFU-04-15 is from A. Mundl (unpublished data) (b) Plot of $\mu^{142}\text{Nd}$ vs. $^3\text{He}/^4\text{He}$ (R/R_A) (Mundl et al., 2017 and references therein). There is no correlation between W or He isotope compositions with Nd isotope compositions. The Samoa sample that shows a small but resolved ^{142}Nd enrichment also has a larger ^{182}W deficit and higher $^3\text{He}/^4\text{He}$, although Loihi samples with ^{182}W deficits and high $^3\text{He}/^4\text{He}$ do not have resolvable different ^{142}Nd .

crust production and recycling. For this assessment, however, the choice of the composition of the bulk-silicate Earth (BSE) is important.

Estimates of the Sm–Nd systematics of the bulk silicate earth (BSE) are usually based on chondritic meteorites, given that both Sm and Nd are refractory lithophile elements. The more primitive of these meteorites that provide the best estimate of Solar System composition show a very narrow range in Sm/Nd ratios and modern day $^{143}\text{Nd}/^{144}\text{Nd}$ (e.g., Jacobsen and Wasserburg, 1980; Bouvier et al., 2008) that form the basis for estimating that the BSE has a $^{147}\text{Sm}/^{144}\text{Nd} = 0.1960$ and present day $^{143}\text{Nd}/^{144}\text{Nd} = 0.512630$ (Bouvier et al., 2008). Estimating the BSE $^{142}\text{Nd}/^{144}\text{Nd}$, however, is not as straightforward. Chondritic meteorites show a range in $\mu^{142}\text{Nd}$ values >30 , with nearly all measured values being lower than modern terrestrial mantle-derived rocks (Boyett and Carlson, 2005; Carlson et al., 2007; Andreason and Sharma, 2006; Gannoun et al., 2011; Burkhardt et al., 2016; Bouvier and Boyet, 2016). Only enstatite chondrites are known to be characterized by $^{142}\text{Nd}/^{144}\text{Nd}$ ratios that overlap with those observed in the modern mantle, and only a small subset of the data for this group extend to ratios as high as Earth's modern mantle. The range in $\mu^{142}\text{Nd}$ values seen in chondrites does not correlate with their Sm/Nd ratios. This observation, coupled with minor variability in other stable Nd isotope ratios, suggests that the majority of the Nd isotopic variability measured in meteorites results from the incorporation of different mixtures of *r*-process and *s*-process Nd produced by different nucleosynthetic processes (Carlson et al., 2007; Burkhardt et al., 2016; Bouvier and Boyet, 2016). A correlation observed between Nd and Mo isotopic compositions in enstatite and ordinary chondrites and the Earth provides evidence that the variability in $\mu^{142}\text{Nd}$ among chondrites is entirely nucleosynthetic in origin, and suggests that the BSE has a $\mu^{142}\text{Nd} = 0.3 \pm 2.6$, if terrestrial Nd and Mo were derived from the same planetary building blocks (Render et al., 2017). On the other hand, enstatite chondrites may have small deficits in $^{142}\text{Nd}/^{144}\text{Nd}$ of a few to several ppm, either with no clearly resolvable anomalies in the other stable Nd isotope ratios (Bouvier and Boyet, 2016) or after small corrections for *s*-process deficits in other stable Nd isotope ratios (Burkhardt et al., 2016). These results, combined, appear to leave open the possibility that the $^{142}\text{Nd}/^{144}\text{Nd}$ of BSE could have deficits of up to several ppm, relative to JNdi.

Despite the uncertainty in the ^{142}Nd composition of the BSE, we can examine the extent to which the ^{142}Nd and ^{143}Nd histories of the samples in this study could be coupled. Fig. 6 shows the modern Nd isotope compositions that would be generated by single episodes of fractionation of Sm/Nd at different times. The black lines show results for fractionation at 4.568 and 4.500 Ga,

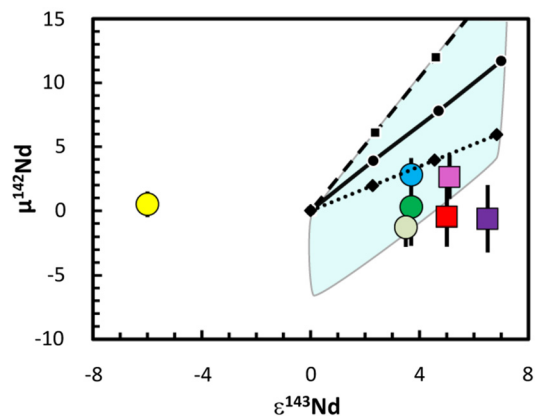


Fig. 6. A comparison of the modern Nd isotope compositions that would be generated by a single episode of melt depletion at 4.568 Ga (dashed black line), at 4.50 Ga (solid black line) and at 4.42 Ga (dotted black line). Starting composition for these calculations is a mantle reservoir with $\mu^{142}\text{Nd}$ and $\epsilon^{143}\text{Nd} = 0$, and $^{147}\text{Sm}/^{144}\text{Nd}$ ratio = 0.196. For $^{147}\text{Sm}/^{144}\text{Nd}$ ratios of 0.196, 0.200, 0.204 and 0.208 after melt depletion, the $\epsilon^{143}\text{Nd}$ and $\mu^{142}\text{Nd}$ grow to those values shown as small black symbols. The enclosed field extends the possible starting composition of BSE to $\mu^{142}\text{Nd} = -7$ (similar to the average for enstatite chondrites) and shows the range of compositions possible for fractionation between 4.568 Ga and 4.500 Ga, within the lifetime of ^{182}Hf . Data for Samoa are shown as circles; samples from Hawaii are squares.

i.e., at the start of Solar System history while ^{182}Hf was still extant, and at 4.42 Ga after ^{182}Hf became extinct. The latter age, an estimate for the timing of primordial differentiation of Earth's mantle based on ^{142}Nd in Archean rocks (e.g., Rizo et al., 2012; Caro et al., 2006; Morino et al., 2017), may represent a minimum differentiation age. These calculations assume that both initial $\mu^{142}\text{Nd}$ and $\epsilon^{143}\text{Nd}$ compositions were 0, and model the effect of extraction of 0.3% to 1% melt from an upper mantle source composed of olivine, orthopyroxene and clinopyroxene. Such melt extraction changes the $^{147}\text{Sm}/^{144}\text{Nd}$ ratio of the residue from 0.1960 to between 0.200 and 0.208, respectively. To accommodate uncertainty in the BSE composition, the blue field in Fig. 6 extends the range of compositions that would be generated by early melt removal between 4.568 and 4.500 Ga in a BSE whose initial $\mu^{142}\text{Nd}$ was between 0 and -7 . The lower value reflects the average $\mu^{142}\text{Nd}$ of enstatite chondrites (Boyett and Carlson, 2005; Carlson et al., 2007; Gannoun et al., 2011; Bouvier and Boyet, 2016; Burkhardt et al., 2016).

Four of the basalts examined here have $\mu^{142}\text{Nd}$ values that are within the ± 1.0 ppm 95% confidence interval of the value of the JNdi standard. The Samoan basalt OFU 04-14 extends the range in

$\mu^{142}\text{Nd}$ to +2.7. The $\varepsilon^{143}\text{Nd}$ of all the samples, except for Samoan basalt ALIA 118-15, are all positive. The combination of positive $\mu^{142}\text{Nd}$ and $\varepsilon^{143}\text{Nd}$ causes most of the basalts to plot to the right of the single-stage differentiation curves shown in Fig. 6 if the BSE has a $\mu^{142}\text{Nd} = 0$. The $\varepsilon^{143}\text{Nd}$ value for Samoan basalt ALIA 118-15 is much lower than the other samples, and possible reasons for this are discussed below. The positive $\varepsilon^{143}\text{Nd}$ values of the remaining samples studied here can be reconciled with $\mu^{142}\text{Nd} = 0$ for BSE if there was a later stage of increase in Sm/Nd ratio after the effective extinction of ^{146}Sm at about 4 Ga. The conventional model for generating the positive $\varepsilon^{143}\text{Nd}$ of the MORB source is through its depletion in incompatible elements as a result of the extraction of incompatible element-rich continental crust throughout Earth history (Jacobsen and Wasserburg, 1979; Allègre et al., 1983). The lower $\varepsilon^{143}\text{Nd}$ of many OIB compared to MORB can then be explained by either contamination of the depleted mantle with recycled crustal materials, or by mixing between depleted and primitive mantle, the latter with $\varepsilon^{143}\text{Nd} \equiv 0$ (Allègre et al., 1983; White, 1985). The $\varepsilon^{143}\text{Nd}$ values of these basalts are consistent with depleted mantle (0.58 ppm Nd, $\varepsilon^{143}\text{Nd} = +10.9$; Workman and Hart, 2005) comprising 50–70% of the mantle source with the rest from primitive mantle (1.25 ppm Nd, $\varepsilon^{143}\text{Nd} = 0$; McDonough and Sun, 1995). The sources for the sample with $\mu^{142}\text{Nd}$ of +2.7 may include not only primitive mantle and MORB-type depleted mantle, but also a mantle domain depleted during the early Hadean. Alternatively, if the BSE has $\mu^{142}\text{Nd} < 0$, then the ^{142}Nd – ^{143}Nd systematics permit that all of these samples, except for the sample from Savai'i that has negative $\varepsilon^{143}\text{Nd}$, were derived, at least in part, from mantle domains that formed during the early Hadean.

A good example of the consequences of the recycling of crustal materials is provided by sample ALIA 118-15, a submarine lava collected off the coast of Savai'i, in western Samoa. This basalt has a far lower $\varepsilon^{143}\text{Nd}$ value than the rest of the samples examined here and that is also substantially subchondritic. The trace element contents, negative $\varepsilon^{143}\text{Nd}$, and radiogenic $^{87}\text{Sr}/^{86}\text{Sr}$ ($=0.7186$) composition of this basalt are consistent with a mantle source that incorporated approximately 5% of a subducted upper continental crust (UCC) component prior to melting (Jackson et al., 2007). Further, this modelling suggests that approximately 40% of the Nd in the basalt melt may have been derived from this UCC endmember (Jackson et al., 2007). Incorporation of this fraction of UCC in the source of the sample apparently had no resolvable effect on ^{142}Nd . Given that a range of about ± 20 ppm in $^{142}\text{Nd}/^{144}\text{Nd}$ is observed in Archean crustal rocks (Caro et al., 2006; Bennett et al., 2007; O'Neil et al., 2008; Rizo et al., 2012, 2013; Morino et al., 2017), mixing of ambient mantle having $\mu^{142}\text{Nd} = 0$ with 40% of a crustal component at the extreme of the compositions measured for Archean crust would produce a melt with $\mu^{142}\text{Nd}$ of ± 8 ppm, which would be well resolved in our data. Most Archean rocks and all post-Archean continental crust measured to date, however, do not show $\mu^{142}\text{Nd}$ values resolved from zero, so the lack of an anomaly in $\mu^{142}\text{Nd}$ in ALIA 118-15 is not surprising. Additional precise ^{142}Nd data on post-Archean continental crust would help to better characterize the possible range of compositions of subducted UCC components.

These examples of ^{142}Nd – ^{143}Nd systematics thus suggest that much of the Nd in these samples has undergone post-Hadean processing during development of depleted mantle or the formation and recycling of continental crust. Dilution of primordial ^{142}Nd variations, then, may help to explain why $^{142}\text{Nd}/^{144}\text{Nd}$ ratios in these samples from Samoa and Hawaii vary by no more than a few ppm. Some mantle domains sampled by these volcanic systems possibly are characterized by much larger ^{142}Nd anomalies, but that heterogeneity could have been attenuated through vigorous mixing in hot plumes during transit to the surface (Jackson et

al., 2017). An alternative possibility is that the mantle sources of these magmas were sufficiently mixed by mantle convection over Earth history as to nearly obliterate the evidence for early differentiation recorded by ^{142}Nd . Debaille et al. (2013) used diminution of ^{142}Nd anomalies in late Archean rocks to argue for the end of a stagnant lid tectonic regime for Earth and the subsequent rapid mixing away of mantle with anomalous ^{142}Nd resulting from the advent of modern plate tectonics. The very small variations ^{142}Nd observed here, therefore, may indicate incomplete homogenization either within the plumes or by long-term mantle convection.

Another possible contributor to limited variation in ^{142}Nd in these sources was insufficient fractionation of Sm/Nd in deep mantle sources while ^{146}Sm was extant. The presence of a range of $\mu^{142}\text{Nd} \pm 20$ in Archean supracrustal rocks argues against this explanation, at least for the likely upper mantle sources of the supracrustal rocks. Crystallization of a basal magma ocean in the presence of Ca-perovskite would be expected to generate domains having heterogeneous Sm/Nd ratios in the solids and residual melts (Hirose et al., 2004; Corgne et al., 2005; Labrosse et al., 2007). If crystallization of the magma ocean occurred after the first 100–200 Ma of Earth history, then sizable ^{142}Nd anomalies may never have been generated in deep mantle domains that may be sampled by modern plumes. Magma ocean differentiation this late in Earth's history also would leave no signature in ^{182}W and ^{129}I because both radioactive parents for these isotopes would have been extinct by 4.45 to 4.50 Ga.

4.2. Constraints on source materials

If the limited range in $\mu^{142}\text{Nd}$ results from mixing with “normal” upper mantle, then it must be explained why the sources of these basalts preserve a far larger range in $^{182}\text{W}/^{184}\text{W}$, which must also have been created early in Earth history. One possible source of high $^3\text{He}/^4\text{He}$ and low $^{182}\text{W}/^{184}\text{W}$ in some Samoa and Hawaii basalts is the core (e.g. Porcelli and Halliday, 2001), although the highly-siderophile-element abundances in these lavas are not easily reconciled with a direct core contribution (Mundl et al., 2017). The lack of appreciable Nd in the core means that no correlation between ^{182}W and ^{142}Nd should be expected to result from core–mantle interaction. To explain the variations in W and He isotope compositions, Mundl et al. (2017) speculated that the Samoa and Hawaii OIB systems access rare, seismically distinct ultralow velocity zones (ULVZ) that may host ancient deficits in ^{182}W and high $^3\text{He}/^4\text{He}$ ratios. These are attractive sites from which to extract the anomalous W and He because the largest ULVZs are located near the core–mantle boundary beneath Hawaii and Samoa (Cottaar and Romanowicz, 2012; Thorne et al., 2013). Further, the seismic profiles of the ULVZ are consistent with the presence of Fe-rich silicate or metallic melt (Rost et al., 2006; Wicks et al., 2010; Mao et al., 2006; Zhang et al., 2016). Early-formed metal, such as generated by disproportionation reactions, that is trapped at the core–mantle boundary would likely be characterized by comparatively high W contents, low Hf/W and may have incorporated the low $\mu^{182}\text{W}$ value of the mantle at the time of its isolation. Such metal might also have incorporated primitive He, characterized by high $^3\text{He}/^4\text{He}$ (Bouhifd et al., 2013). Finally, in addition to overlying ULVZ, the plumes associated with the Hawaii and Samoa hotspots simultaneously have high hotspot buoyancy fluxes, high upper mantle temperatures and produce basalts with high $^3\text{He}/^4\text{He}$ ratios (Jackson et al., 2017). As the hottest and most buoyant plumes, they, therefore, may be best able to entrain dense mantle domains residing near the core mantle boundary that, as a result of their density, are ideally suited for preserving early-formed reservoirs (Mukhopadhyay, 2012; Rizo et al., 2016; Jackson et al., 2017; Mundl et al., 2017). If the Samoan and Hawaiian ^{182}W and $^3\text{He}/^4\text{He}$ anomalies are attributed to contributions to the plumes from pri-

mordial metal, then nonmetallic components in the ULVZ might contribute the small ^{142}Nd anomalies. The small magnitude of the ^{142}Nd variation may then relate either to limited Sm/Nd fractionation in the ULVZ material, or to Nd concentrations that are not high enough to imprint their isotopic signature on the other components present in the plume that supplied the volcanism at these hot spots.

The only previous study of combined ^{182}W and ^{142}Nd in relatively young basalts examined two picrites from the Baffin Bay area and a basalt from the Ontong Java plateau. The Baffin Bay area hosts basalts that are considered to be an early manifestation of Iceland plume volcanism and have the highest $^3\text{He}/^4\text{He}$ measured for any mantle-derived modern basalt (Stuart et al., 2003). Lavas from the Ontong Java Plateau, the largest terrestrial volcanic province, sample a mantle source with a primitive Pb-isotopic composition, similar to those from the Baffin Bay area (Jackson and Carlson, 2011). These samples, as well as an additional suite of basalts from same area, have $\mu^{142}\text{Nd}$ values within 8 ppm of JNdI, but the data are not sufficiently precise to resolve whether there is variation within this suite (Rizo et al., 2016; de Leeuw et al., 2017). Rizo et al. (2016) reported elevated $^{182}\text{W}/^{184}\text{W}$ ratios in basalts from both localities, in contrast with the depleted $^{182}\text{W}/^{184}\text{W}$ compositions of the OIB samples examined here. These differences in ^{182}W are perhaps indicative that several sources with distinct early-Earth histories are involved in oceanic basalt genesis.

5. Conclusions

The data reported here support the presence of a limited range of $^{142}\text{Nd}/^{144}\text{Nd}$ in ocean island basalts from Samoa and Hawaii. A small difference is resolved between two samples from the Samoa hotspot which, given the half-life of ^{146}Sm , implies preservation of Hadean silicate differentiation events in the modern mantle. These samples show considerably variable and mostly negative $\mu^{182}\text{W}$ (Mundl et al., 2017), in contrast to young oceanic basalts from Baffin Island and the Ontong Java plateau that have positive $\mu^{182}\text{W}$ (Rizo et al., 2016). No single process can account for these observations. Any correlation between $^{182}\text{W}/^{184}\text{W}$ and $^{142}\text{Nd}/^{144}\text{Nd}$ is limited, which likely indicates that different processes and different materials were involved in the generation of the Nd and W anomalies. Early differentiation that included core–mantle segregation and mantle outgassing would dramatically affect W and He isotope evolution, respectively. The more subdued signal in $\mu^{142}\text{Nd}$ could reflect more limited early Hadean differentiation of the silicate portion of the Earth, greater homogenization during mantle convection or upwelling, or overprinting by recycled crustal components.

The search for modern ^{142}Nd anomalies should continue, especially coupled with ^{182}W data on the same samples. Better characterization of the ^{142}Nd composition of the convecting upper mantle through more precise analysis of MORB, and the secular variation in upper continental crust as recorded in sedimentary rocks, would be particularly useful. Replicate dissolutions and analyses of individual samples offer a promising way to resolve small variations of ^{142}Nd in young rocks.

Acknowledgements

We are grateful to A. Mundl, B. Peters, J. Reimink and S.B. Shirey for discussions, and to T. Mock for maintaining the mass spectrometers in peak condition. We thank M. Garcia and M. Kurz for providing samples, and A. Mundl for sharing her unpublished W isotope data on sample OFU-04-15. E. Hoffmann and an anonymous reviewer provided helpful comments. We thank F. Moynier

for editorial assistance. This work was funded by the Carnegie Institution for Science.

Appendix A. Supplementary material

Supplementary material related to this article can be found online at <https://doi.org/10.1016/j.epsl.2017.12.017>.

References

- Allège, et al., 1983. Chemical structure and evolution of the mantle and continents determined by inversion of Nd and Sr isotopic data, II. Numerical experiments and discussion. *Earth Planet. Sci. Lett.* 66, 191–231.
- Andreasen, R., Sharma, M., 2006. Solar nebula heterogeneity in p-process samarium and neodymium isotopes. *Science* 314, 806–809.
- Bennett, V.C., Brandon, A.D., Nutman, A.P., 2007. Coupled ^{142}Nd – ^{143}Nd isotopic evidence for Hadean mantle dynamics. *Science* 318, 1907–1910.
- Bouhifd, M.A., Jephcoat, A.P., Heber, V.S., Kelley, S.P., 2013. Helium in the Earth's core. *Nature* 6, 982–986.
- Bouvier, A., Vervoort, J.D., Patchett, P.J., 2008. The Lu–Hf and Sm–Nd isotopic composition of CHUR: constraints from unequilibrated chondrites and implications for the bulk composition of terrestrial planets. *Earth Planet. Sci. Lett.* 273, 48–57.
- Bouvier, A., Boyet, M., 2016. Primitive solar system materials and Earth share a common initial ^{142}Nd abundance. *Nature* 537, 399–402.
- Boyet, M., Carlson, R.W., 2005. ^{142}Nd evidence for early (>4.53 Ga) global differentiation of the silicate Earth. *Science* 309, 576–581.
- Boyet, M., Carlson, R.W., 2006. A new geochemical model for the Earth's mantle inferred from ^{146}Sm – ^{142}Nd systematics. *Earth Planet. Sci. Lett.* 250, 254–268.
- Burkhardt, C., Borg, L.E., Brennecka, G.A., Shollenberger, Q.R., Dauphas, N., Kleine, T., 2016. A nucleosynthetic origin for the Earth's anomalous ^{142}Nd composition. *Nature* 537, 394–398.
- Carlson, R.W., Boyet, M., Horan, M., 2007. Chondrite barium, neodymium, and samarium isotopic heterogeneity and early Earth differentiation. *Science* 316, 1175–1178.
- Caro, G., Bourdon, B., Birck, J.L., Moorbath, S., 2006. High precision $^{142}\text{Nd}/^{144}\text{Nd}$ measurements in terrestrial rocks: constraints on the early differentiation of the Earth's mantle. *Geochim. Cosmochim. Acta* 70, 164–191.
- Coltice, N., Moreira, M., Hernlund, J., Labrosse, S., 2011. Crystallization of a basal magma ocean recorded by helium and neon. *Earth Planet. Sci. Lett.* 308, 193–199.
- Corgne, A., Liebske, C., Wood, B.J., Rubie, D., Frost, D.J., 2005. Silicate perovskite–melt partitioning of trace elements and geochemical signature of a deep perovskitic reservoir. *Geochim. Cosmochim. Acta* 69, 485–496.
- Cottaar, S., Romanowicz, B., 2012. An unusually large ULVZ at the base of the mantle near Hawaii. *Earth Planet. Sci. Lett.* 355–356, 213–222.
- de Leeuw, G.A.M., Ellam, R.M., Stuart, F.M., Carlson, R.W., 2017. $^{142}\text{Nd}/^{144}\text{Nd}$ inferences on the nature and origin of the source of high $^3\text{He}/^4\text{He}$ magmas. *Earth Planet. Sci. Lett.* 472, 62–68.
- Debaille, V., O'Neill, C.O., Brandon, A.D., Haenecour, P., Yin, Q.-Z., Mattielli, N., Treiman, A.H., 2013. Stagnant lid tectonics in early Earth revealed by ^{142}Nd variation in late Archean rocks. *Earth Planet. Sci. Lett.* 373, 83–92.
- Gannoun, A., Boyet, M., Rizo, H., Goresy, A.E., 2011. ^{146}Sm – ^{142}Nd systematics measured in enstatite chondrites reveals a heterogeneous distribution of ^{142}Nd in the solar nebula. *Proc. Natl. Acad. Sci.* 108, 7693–7697.
- Hirahara, Y., Chang, Q., Miyazaki, T., Takahashi, T., Kimura, J., 2012. Improved Nd chemical separation technique for $^{143}\text{Nd}/^{144}\text{Nd}$ analysis in geological samples using packed Ln resin columns. *JAMSTEC Rep. Res. Dev.* 15, 27–33.
- Hirose, K., Shimizu, N., van Westernen, W., Fei, Y., 2004. Trace element partitioning in Earth's lower mantle and implications for geochemical consequences of partial melting at the core–mantle boundary. *Phys. Earth Planet. Inter.* 146, 249–260.
- Jackson, M.G., Hart, S.R., Koppers, A., Staudigal, H., Konter, J., Blusztajn Kurz, M., Russell, J.A., 2007. The return of subducted continental crust in Samoan lavas. *Nature* 448, 685–687.
- Jackson, M.G., Carlson, R.W., 2011. An ancient recipe for flood basalt genesis. *Nature*. <https://doi.org/10.1038/nature10326>.
- Jackson, M.G., Carlson, R.W., 2012. Homogeneous superchondritic $^{142}\text{Nd}/^{144}\text{Nd}$ in the mid-ocean ridge basalt and ocean island basalt mantle. *Geochim. Geophys. Geosyst.* 13, Q06011. <https://doi.org/10.1029/2012GC004114>.
- Jackson, M.G., Konter, J.G., Becker, T.W., 2017. Primordial He entrained by the hottest mantle plumes. *Nature*. <https://doi.org/10.1038/nature21023>.
- Jacobsen, S.B., Wasserburg, G.J., 1979. The mean age of mantle and crustal reservoirs. *J. Geophys. Res.* 84, 7411–7427.
- Jacobsen, S.B., Wasserburg, G.J., 1980. Sm–Nd isotopic evolution of chondrites. *Earth Planet. Sci. Lett.* 50, 139–155.
- Labrosse, S., Hernlund, J.W., Coltice, N., 2007. A crystallizing dense magma ocean at the base of the Earth's mantle. *Nature* 450, 866–869.
- Ludwig, K.R., 2008. User's manual for Isoplot 3.70: a geochronological toolkit for Microsoft Excel. *Berkley Geochronology Center Spec. Pub.* 4. 76 pp.

- Mao, W., Mao, H., Sturhahn, W., Zhao, J., Prakapenka, V., Yue, M., Shu, J., Fei, Y., Hemley, R., 2006. Iron-rich post-perovskite and the origin of ultralow velocity zones. *Science* 312, 564–565.
- McDonough, W.F., Sun, S.S., 1995. The composition of the Earth. *Chem. Geol.* 120, 223–253.
- Morino, P., Caro, G., Reisberg, L., Schumacher, A., 2017. Chemical stratification in the post-magma ocean Earth inferred from coupled $^{146,147}\text{Sm}$ – $^{142,143}\text{Nd}$ systematics in ultramafic rocks of the Saglek block (3.25–3.9 Ga) northern Labrador, Canada. *Earth Planet. Sci. Lett.* 3, 136–150.
- Mukhopadhyay, S., 2012. Early differentiation and volatile accretion in deep mantle neon and xenon. *Nature* 486, 101–104.
- Mundl, A., Touboul, M., Jackson, M.G., Day, J.M.D., Kurz, M.D., Lekic, V., Helz, R.T., Walker, R.J., 2017. Tungsten-182 heterogeneity in modern ocean island basalts. *Science* 356, 66–69.
- Murphy, D.T., Brandon, A.D., Debaille, V., Burgess, R., 2010. In search of a hidden long-term isolated sub-chondritic $^{142}\text{Nd}/^{144}\text{Nd}$ reservoir in the deep mantle: implications for the Nd isotope systematics of the Earth. *Geochem. Cosmochim. Acta* 74, 738–750.
- NIST/SEMATECH, 2012. Engineering statistics: NIST/SEMATECH e-Handbook of statistical methods. <http://www.itl.nist.gov/div898/handbook/>.
- O'Neil, J., Carlson, R.W., Francis, D., Stevenson, R.K., 2008. Neodymium-142 evidence for Hadean mafic crust. *Science* 321, 1828–1831.
- Parai, R., Mukhopadhyay, S., 2015. The evolution of MORB and plume mantle volatile budgets: constraints from fission Xe isotopes in Southwest Indian Ridge basalts. *Geochem. Geophys. Geosyst.* 16, 719–735. <https://doi.org/10.1002/2014GC005566>.
- Petó, M.K., Mukhopadhyay, S., Kelley, K.A., 2013. Heterogeneities from the first 100 million years recorded in deep mantle noble gases from the Northern Lau Back-arc Basin. *Earth Planet. Sci. Lett.* 369, 13–23.
- Porcelli, D., Halliday, A.N., 2001. The core as a possible source of mantle helium. *Earth Planet. Sci. Lett.* 192, 45–56.
- Render, J., Fischer-Goedde, M., Burkhardt, C., Kleine, T., 2017. The cosmic molybdenum–neodymium isotope correlation and the building material of the Earth. *Geochem. Perspect. Lett.* 3, 170–178.
- Rizo, H., Boyet, M., Blichert-Toft, J., O'Neil, J., Rosing, M.T., Paquette, J.-L., 2012. The elusive Hadean enriched reservoir revealed by ^{142}Nd deficits in Isua Archean rocks. *Nature* 491, 96–100. <https://doi.org/10.1038/nature11565>.
- Rizo, H., Boyet, M., Blichert-Toft, J., Rosing, M.T., 2013. Early mantle dynamics inferred from ^{142}Nd variations in Archean rocks from southwest Greenland. *Earth Planet. Sci. Lett.* 377, 324–335.
- Rizo, H., Walker, R.J., Carlson, R.W., Horan, M.F., Mukhopadhyay, S., Manthos, V., Francis, D., Jackson, M.G., 2016. Preservation of Earth-forming events in the tungsten isotopic composition of modern flood basalts. *Science* 352, 809–812.
- Rost, S., Garnero, E.J., Williams, Q., 2006. Fine scale ultralow velocity zone structure from high frequency seismic array data. *J. Geophys. Res.* 111, B09310. <https://doi.org/10.1029/2005JB004088>.
- Stuart, F.M., Lass-Evans, S., Fitton, J.G., Ellam, R.M., 2003. High $^3\text{He}/^4\text{He}$ ratios in picritic basalts from Baffin Island and the role of a mixed reservoir in mantle plumes. *Nature* 424, 57–59.
- Thorne, M.S., Garnero, E.J., Janke, G., Heiner, I., McNamara, A.K., 2013. Mega ultra low velocity zone and mantle flow. *Earth Planet. Sci. Lett.* 364, 59–67.
- White, W.W., 1985. Sources of oceanic basalts: radiogenic isotopic evidence. *Geology* 13, 115–118.
- Wicks, J.K., Jackson, J.M., Sturhahn, W., 2010. Very low sound velocities in iron-rich (Mg, Fe)O: implications for the core–mantle boundary region. *Geophys. Res. Lett.* 37, L15304. <https://doi.org/10.1029/2010GL043689>.
- Willbold, M., Elliott, T., Moorbath, S., 2011. The tungsten isotopic composition of the Earth's mantle before the terminal bombardment. *Nature* 477, 195–198.
- Workman, R.K., Hart, S.R., 2005. Major and trace elements composition of the depleted MORB mantle (DMM). *Earth Planet. Sci. Lett.* 231, 53–72.
- Zhang, Z., Dorfman, S.M., Labidi, J., Zhang, S., Li, M., Manga, M., Stixrude, L., McDonough, W.F., Williams, Q., 2016. Primordial metallic melt in the deep mantle. *Geophys. Res. Lett.* 43. <https://doi.org/10.1002/2016GL068560>.